

Spin-induced Scalarized Black Holes in Einstein-Maxwell-scalar Models

Lang Cheng^{a,*}, Guangzhou Guo^{b,a,†}, Peng Wang^{a,‡} and Haitang Yang^{a,§}

^a*Center for Theoretical Physics, College of Physics,
Sichuan University, Chengdu, 610064, China and*

^b*Department of Physics, Southern University of Science and Technology, Shenzhen, 518055, China*

We construct spin-induced scalarized black hole solutions in a class of Einstein-Maxwell-scalar models, where a scalar field is non-minimally coupled to the electromagnetic field. Our results show that scalar hair develops only for rapidly rotating black holes, while slowly spinning ones remain well described by the Kerr-Newman (KN) metric. The scalar field contributes only a small fraction of the total mass, indicating suppressed nonlinear effects. This suppression may account for the narrow existence domains of scalarized black holes and the similarities observed in their existence domains across different coupling functions. Moreover, scalarized black holes are found to coexist with linearly stable, entropically favored KN black holes. These results motivate further investigations into the nonlinear dynamics and stability of scalarized black holes in these models.

arXiv:2506.01773v1 [gr-qc] 2 Jun 2025

* chenglang@stu.scu.edu.cn

† guogz@sustech.edu.cn

‡ pengw@scu.edu.cn

§ hyanga@scu.edu.cn

CONTENTS

I. Introduction		2
II. Setup		4
A. Einstein-Maxwell-scalar Models		4
B. Rotating Black Hole Solutions		5
III. Numerical Results		8
IV. Conclusions		12
Acknowledgments		13
A. Convergence Tests		13
B. Quadratic Coupling Function		15
References		15

I. INTRODUCTION

Recently, the LIGO and Virgo Collaborations reported the detection of gravitational waves from binary black hole mergers [1], while the Event Horizon Telescope Collaboration produced the first images of the supermassive black holes M87* and Sgr A* [2–15]. These groundbreaking observations have opened new avenues for testing general relativity in the strong-field regime, including the no-hair theorem, which asserts that stationary black holes are uniquely characterized by their mass, angular momentum and charge [16–18]. However, counterexamples to the no-hair theorem—commonly referred to as “hairy” black holes—have been found in various theories, where black holes possess additional degrees of freedom. The first such solutions were discovered in the Einstein-Yang-Mills theory [19–21]. Subsequently, black hole solutions with Skyrme hair [22, 23] and dilaton hair [24] were also obtained. For a comprehensive review, see [25].

Recently, the no-hair theorem has been challenged by extended theories of gravity that introduce non-minimal couplings between scalar fields and other fundamental fields. A prominent mechanism for circumventing this theorem is spontaneous scalarization, wherein a trivial scalar field configuration around a black hole becomes unstable and evolves into a non-trivial configuration, leading

to the emergence of scalar hair [26–29]. This phenomenon is typically driven by a tachyonic instability, in which scalar field perturbations acquire an effective negative mass squared on the black hole background, triggering growth of the scalar field. In particular, it has been demonstrated that in Einstein-scalar-Gauss-Bonnet (EsGB) theories, a scalar field appropriately coupled to the Gauss-Bonnet invariant can develop a tachyonic instability near Kerr black holes when the spin exceeds a critical threshold [30]. This spin-induced instability has subsequently been shown to lead to the formation of spin-induced scalarized black holes at sufficiently high spins [31, 32].

To gain deeper insight into the dynamical evolution of scalarization, a technically simpler class of models known as Einstein-Maxwell-scalar (EMS) models has been proposed [33]. In these models, a scalar field is non-minimally coupled to the electromagnetic sector, enabling scalarized black hole solutions that go beyond Kerr-Newman (KN) solutions [34–39]. Remarkably, scalarized black holes in the EMS models can exhibit multiple light rings in the equatorial plane [39, 40]. This feature not only leads to distinctive optical signatures in black hole imaging [41–45] but is also associated with the existence of long-lived quasinormal modes [46–50] and potential superradiant instabilities [51].

While most studies of the EMS models have focused on positive scalar-electromagnetic coupling constants—where scalarization is typically driven by electric charge—recent work has shown that, for sufficiently negative coupling constants, rapidly rotating KN black holes can also undergo spontaneous scalarization triggered by a spin-induced instability [52, 53]. Furthermore, the domain of existence for scalar clouds arising from this spin-induced instability has been thoroughly investigated in the KN black hole parameter space [54]. These scalar clouds are generally interpreted as signaling the onset of spin-induced scalarized KN black holes.

In this paper, we numerically construct spin-induced scalarized KN black hole solutions in the EMS models. The structure of the paper is as follows. In Sec. II, we review the EMS models and describe numerical methods used to obtain scalarized black hole solutions. Sec. III presents numerical results for the spin-induced scalarized KN black holes. A summary of our findings is given in Sec. IV. Finally, Appendix A provides a convergence analysis of the numerical solutions, and Appendix B explores the domain of existence for spin-induced scalarized KN black holes with a quadratic coupling function. Throughout this work, we adopt the convention $G = c = 4\pi\epsilon_0 = 1$.

II. SETUP

In this section, we first review the EMS models that exhibit a tachyonic instability in KN black holes. We then present the numerical method used to construct scalarized KN black hole solutions within these models.

A. Einstein-Maxwell-scalar Models

In the EMS models, a scalar field is non-minimally coupled to electromagnetism, potentially inducing a tachyonic instability in KN black holes. The action for this system is

$$S = \frac{1}{16\pi} \int d^4x \sqrt{-g} [R - 2\partial_\mu \phi \partial^\mu \phi - f(\phi) F^{\mu\nu} F_{\mu\nu}], \quad (1)$$

where R is the Ricci scalar, ϕ is the scalar field, and $F_{\mu\nu} = \partial_\mu A_\nu - \partial_\nu A_\mu$ denotes the electromagnetic field tensor. Varying the action (1) yields the equations of motion for the metric $g_{\mu\nu}$, scalar field ϕ and electromagnetic field A_μ :

$$\begin{aligned} R_{\mu\nu} - \frac{1}{2} R g_{\mu\nu} &= 2T_{\mu\nu}, \\ \square\phi - \frac{\alpha}{2} \phi e^{\alpha\phi^2} F^{\mu\nu} F_{\mu\nu} &= 0, \\ \partial_\mu \left(\sqrt{-g} e^{\alpha\phi^2} F^{\mu\nu} \right) &= 0, \end{aligned} \quad (2)$$

with the energy-momentum tensor

$$T_{\mu\nu} = \partial_\mu \phi \partial_\nu \phi - \frac{1}{2} g_{\mu\nu} (\partial\phi)^2 + e^{\alpha\phi^2} \left(F_{\mu\rho} F_\nu{}^\rho - \frac{1}{4} g_{\mu\nu} F_{\rho\sigma} F^{\rho\sigma} \right). \quad (3)$$

To allow for spontaneous scalarization of KN black holes, the KN black hole solution with $\phi = 0$ must satisfy the equations of motion (2). This requirement imposes a condition on the coupling function $f(\phi)$, specifically $f'(0) = df(\phi)/d\phi|_{\phi=0} = 0$. Without loss of generality, we set $f(0) = 1$. Consequently, $f(\phi)$ can be expanded around $\phi = 0$ as

$$f(\phi) = 1 + \alpha\phi^2 + \mathcal{O}(\phi^3), \quad (4)$$

where α is a dimensionless coupling constant governing the scalar-electromagnetic interaction strength.

In the EMS models, KN black holes exhibit stability against metric and vector perturbations, similar to the Einstein-Maxwell theory [55]. However, they may develop a tachyonic instability when subjected to scalar perturbation $\delta\phi$, leading to the formation of scalarized black holes.

Linearizing the scalar field equation in the KN black hole background yields

$$(\square - \mu_{\text{eff}}^2) \delta\phi = 0, \quad (5)$$

where the effective mass squared is given by $\mu_{\text{eff}}^2 = \alpha F^{\mu\nu} F_{\mu\nu}$. In the Boyer-Linquist coordinates, for a KN black hole with ADM mass M , angular momentum J and electric charge Q , the effective mass squared is given by

$$\mu_{\text{eff}}^2 = -\frac{\alpha Q^2 (r^4 - 6a^2 r^2 \cos^2 \theta + a^4 \cos^4 \theta)}{(r^2 + a^2 \cos^2 \theta)^4}, \quad (6)$$

where $a = J/M$ is the ratio of angular momentum to mass. A tachyonic instability could arise when $\mu_{\text{eff}}^2 < 0$, potentially driving the system away from KN black hole solutions. For $\alpha > 0$, regions where $\mu_{\text{eff}}^2 < 0$ consistently appear outside the event horizon in KN black holes, although these regions shrink as the black hole spin increases [56]. Conversely, when $\alpha < 0$, the $\mu_{\text{eff}}^2 < 0$ regions emerge only when the black hole spin is sufficiently large [54].

However, the condition $\mu_{\text{eff}}^2 < 0$ is only a necessary condition for the appearance of tachyonic instability. To overcome dissipation through the event horizon and spatial infinity, μ_{eff}^2 must be sufficiently negative to induce this instability. In other words, only KN black holes for which μ_{eff}^2 falls below certain threshold values can develop a tachyonic instability. At these thresholds, the tachyonic instability triggers the formation of stationary scalar clouds—regular bound-state solutions to Eq. (5)—that exist outside KN black holes. These scalar clouds mark bifurcation points in the parameter space and signal the onset of scalarized KN black holes. The existence domains for scalar clouds at both fundamental and excited states have been identified for $\alpha > 0$ [56] and $\alpha < 0$ [54], respectively. It is important to note that the existence domains of these scalar clouds are independent of the specific form of the coupling function $f(\phi)$, provided it satisfies the series expansion given in Eq. (4).

B. Rotating Black Hole Solutions

To construct scalarized KN black hole solutions, we employ a generic ansatz for stationary, axisymmetric and asymptotically-flat black hole solutions [31, 39, 57, 58]:

$$ds^2 = -e^{2F_0} N dt^2 + e^{2F_1} \left(\frac{dr^2}{N} + r^2 d\theta^2 \right) + e^{2F_2} r^2 \sin^2 \theta \left(d\varphi^2 - \frac{W}{r^2} dt \right)^2, \\ A_\mu dx^\mu = \left(A_t - A_\varphi \frac{W}{r^2} \sin \theta \right) dt + A_\varphi \sin \theta d\varphi \text{ and } \phi = \phi(r, \theta). \quad (7)$$

Here $N \equiv 1 - r_H/r$, where r_H is the black hole horizon radius. The seven functions $F_0, F_1, F_2, W, A_t, A_\varphi$ and ϕ depend only on the coordinates r and θ .

In the stationary spacetime, two Killing vectors ∂_t and ∂_φ are present. Their linear combination $\xi = \partial_t + \Omega_H \partial_\varphi$, where Ω_H is the angular velocity of the black hole horizon, is null and orthogonal to the horizon. The surface gravity κ is then defined by $\kappa^2 = -(\nabla_\mu \xi_\nu)(\nabla^\mu \xi^\nu)/2$ and related to the Hawking temperature T_H as [57]

$$T_H = \frac{\kappa}{2\pi} = \frac{1}{4\pi r_H} e^{F_0(r_H, \theta) - F_1(r_H, \theta)}. \quad (8)$$

In the EMS models, the black hole entropy is expressed as $S = A_H/4$, where the area of the horizon A_H is given by

$$A_H = 2\pi r_H^2 \int_0^\pi d\theta \sin \theta e^{F_1(r_H, \theta) + F_2(r_H, \theta)}. \quad (9)$$

Various physical quantities, including the black hole mass M , charge Q , angular momentum J , electrostatic potential Φ and horizon angular velocity Ω_H , can be extracted by analyzing the asymptotic behavior of the metric and gauge field functions near the horizon and at spatial infinity [57, 58]:

$$\begin{aligned} A_t|_{r=r_H} &\sim 0, & W|_{r=r_H} &\sim r_H^2 \Omega_H, \\ A_t|_{r=\infty} &\sim \Phi - \frac{Q}{r}, & W|_{r=\infty} &\sim \frac{2J}{r}, & e^{2F_0} N|_{r=\infty} &\sim 1 - \frac{2M}{r}. \end{aligned} \quad (10)$$

These quantities further satisfy the Smarr relation [38, 57, 59]:

$$M = 2T_H S + 2\Omega_H J + \Phi Q, \quad (11)$$

which allows us to assess the accuracy of our numerical solutions.

To obtain scalarized black hole solutions, we numerically solve the coupled partial differential equations derived by substituting the ansatz in Eq. (7) into the equations of motion (2). For numerical implementation, we compactify the radial coordinate r via the transformation

$$x = \frac{\sqrt{r^2 - r_H^2} - r_H}{\sqrt{r^2 - r_H^2} + r_H}, \quad (12)$$

which maps the event horizon $r = r_H$ and spatial infinity $r = \infty$ to $x = -1$ and $x = 1$. Using this compactified coordinate x , the power series expansions near the horizon yield the following boundary conditions at $x = -1$:

$$\partial_x F_0 = \partial_x F_1 = \partial_x F_2 = \partial_x \phi = \partial_x A_\varphi = A_t = W - \Omega_H = 0. \quad (13)$$

Meanwhile, boundary conditions at $x = 1$ are obtained by imposing flatness at spatial infinity:

$$F_0 = F_1 = F_2 = \phi = A_\varphi = A_t - \Phi = W = 0. \quad (14)$$

On the symmetric axis, axial symmetry and regularity impose the following conditions at $\theta = 0$ and $\theta = \pi$:

$$\partial_\theta F_0 = \partial_\theta F_1 = \partial_\theta F_2 = \partial_\theta \phi = \partial_\theta A_\varphi = \partial_\theta A_t = \partial_\theta W = 0. \quad (15)$$

In this work, we focus on solutions exhibiting equatorial-plane symmetry, allowing us to restrict the computational domain to the upper half-plane $0 \leq \theta \leq \pi/2$. Consequently, the $\theta = \pi$ boundary condition in Eq. (15) is replaced with

$$\partial_\theta F_0 = \partial_\theta F_1 = \partial_\theta F_2 = \partial_\theta \phi = \partial_\theta A_\varphi = \partial_\theta A_t = \partial_\theta W = 0 \text{ at } \theta = \pi/2. \quad (16)$$

Consequently, Eqs. (13), (14), (15) and (16) serve as the boundary conditions for solving the partial differential equations. Additionally, the absence of conical singularities imposes $F_1 = F_2$ on the symmetry axis, which provides an independent consistency check for our numerical results alongside the Smarr relation [31, 57].

This work employs spectral methods to numerically solve the coupled nonlinear partial differential equations governing the system. Spectral methods are well-established and particularly effective for solving nonlinear elliptic partial differential equations. They approximate solutions using a finite linear combination of basis functions, thereby transforming the differential equations into a system of algebraic equations. A key advantage of spectral methods is their exponential convergence rate with increasing resolution, which far exceeds the linear or polynomial convergence characteristic of finite difference or finite element methods.

In our numerical work, we implement spectral methods by approximating the functions of interest, collectively denoted by $\mathcal{F} = \{F_0, F_1, F_2, W, A_t, A_\varphi, \phi\}$, as a finite linear combination of basis functions:

$$\mathcal{F}^{(k)} = \sum_{i=0}^{N_x-1} \sum_{j=0}^{N_\theta-1} a_{ij}^{(k)} T_i(x) \cos(2j\theta), \quad (17)$$

where $T_i(x)$ represents the i -th Chebyshev polynomial, $a_{ij}^{(k)}$ are the spectral coefficients, and N_x and N_θ denote the resolutions in the radial and angular coordinates, respectively. To determine $a_{ij}^{(k)}$, we substitute the spectral expansions (17) into the equations of motion and then discretize the resulting equations at the Gauss-Chebyshev points. This process transforms the partial differential equations for $\mathcal{F}^{(k)}$ into a finite system of algebraic equations for $a_{ij}^{(k)}$. These algebraic equations

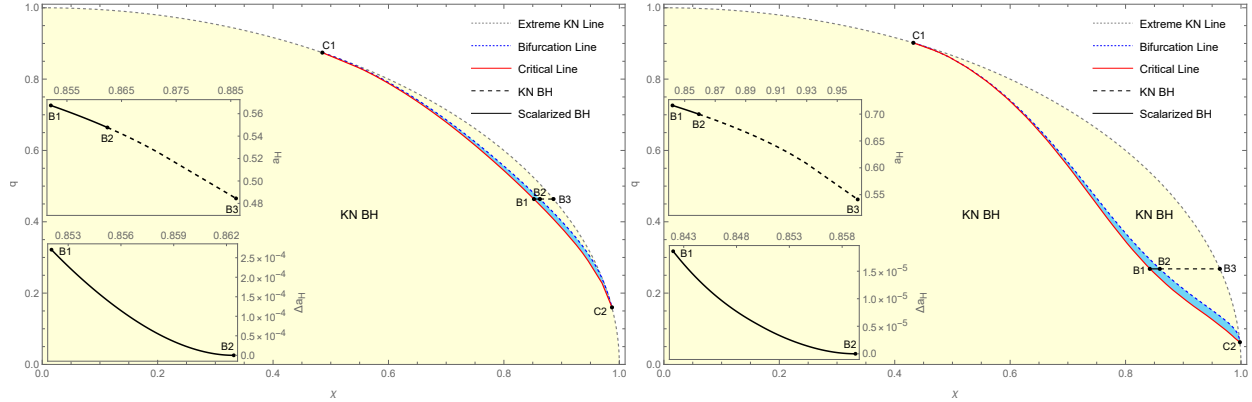


FIG. 1. Domain of existence for spin-induced scalarized KN black holes in the (χ, q) parameter space. **Left Panel:** $\alpha = -100$. **Right Panel:** $\alpha = -1000$. The light yellow region indicates the parameter space of KN black holes, bounded by the extremal KN line corresponding to $q^2 + \chi^2 = 1$. The light blue region denotes the domain of existence for scalarized black holes, within which both KN and scalarized solutions coexist. This domain is bounded by the bifurcation line (blue dashed), where scalarized black holes branch off from KN black holes, and the critical line (red solid), beyond which scalarized black holes can no longer be obtained numerically. Toward both ends of the existence domain, the extremal KN line, bifurcation line and critical line converge and merge at the critical points C_1 and C_2 . The marked points B_1 , B_2 and B_3 on constant- q lines represent a critical scalarized black hole, a bifurcating KN black hole and an extremal KN black hole, respectively. The upper inset shows the reduced horizon area a_H as a function of χ along the constant- q line connecting B_1 and B_3 . The lower inset displays Δa_H , the difference in a_H between KN and scalarized black holes, also as a function of χ . The black dashed line traces KN black hole solutions, while the black solid line corresponds to scalarized black holes.

are then solved using the Newton-Raphson method, with the root-finding process carried out using Mathematica's built-in LinearSolve function.

III. NUMERICAL RESULTS

In this section, we first identify the domain of existence for spin-induced scalarized KN black holes and subsequently analyze their properties. As previously discussed, stationary scalar clouds around KN black holes emerge for $\alpha < 0$ when the black hole spin exceeds a critical threshold. Consequently, we focus on the $\alpha < 0$ regime to construct spin-induced scalarized solutions. For the coupling function, we employ the exponential form $f(\phi) = e^{\alpha\phi^2}$ throughout this section. For comparison, a quadratic coupling function $f(\phi) = 1 + \alpha\phi^2$ is examined in Appendix B. Additionally, we restrict our attention to fundamental black hole solutions, characterized by a nodeless scalar field.

In Appendix A, we conduct convergence tests of scalarized black hole solutions by monitoring the Smarr relation and the absence of conical singularities for varying resolutions, N_x or N_θ . As anticipated, the convergence tests demonstrate exponential convergence as the resolution increases, persisting until a roundoff plateau is reached. To ensure numerical precision and efficiency, we employ spectral methods with resolutions $N_x = 40$ and $N_\theta = 11$ to solve the partial differential equations. With these resolutions, our results indicate that the numerical error of scalarized black hole solutions is less than 10^{-8} when they are sufficiently distant from the critical line. However, as we approach the critical line, the solutions exhibit a numerical error on the order of 10^{-5} . For convenience, we introduce dimensionless reduced quantities $q \equiv Q/M$, $\chi \equiv J/M^2$ and $a_H \equiv A_H/16\pi M$ in the remainder of this section.

Fig. 1 displays the domain of existence for spin-induced scalarized KN black holes in the (χ, q) parameter space, with $\alpha = -100$ (left panel) and $\alpha = -1000$ (right panel). The light blue region, bounded by the bifurcation and critical lines, marks the parameter space where scalarized black holes exist. The bifurcation line corresponds to the threshold at which the tachyonic instability triggers the formation of stationary scalar cloud around KN black holes. Both endpoints, C_1 and C_2 , of the bifurcation line lie on the extremal KN black hole line, defined by $q^2 + \chi^2 = 1$. Starting from the bifurcation line, scalarized black hole solutions are computed along constant- χ lines by varying q until reaching the critical line. Beyond this line, numerical solutions cannot be reliably obtained with an error below 10^{-5} . Interestingly, our numerical results show that the critical line asymptotically approaches both endpoints of the bifurcation line, implying that the bifurcation and critical lines merge at C_1 and C_2 . This indicates that spin-induced scalarized KN black holes do not exist when the spin is either too low or too high. Furthermore, Fig. 1 illustrates that the existence domain expands as $|\alpha|$ increases.

As shown in [54], KN black holes below the bifurcation line are stable against the scalar perturbation, while those above exhibit a tachyonic instability. Therefore, Fig. 1 demonstrates that spin-induced scalarized KN black holes coexist with stable KN black holes possessing the same q and χ within their domain of existence. To examine the behavior of the horizon area, we highlight three distinct black hole configurations with the same q in Fig. 1: B_1 , a critical scalarized black hole; B_2 , a black hole on the bifurcation line; B_3 , an extremal KN black hole. The upper insets show that the reduced horizon area a_H of scalarized black holes decreases as the spin increases for fixed q . The lower insets display Δa_H , the difference in reduced horizon area between KN and scalarized black holes, along the constant- q line connecting B_1 and B_2 . These results indicate that KN black holes generally have a larger reduced horizon area than scalarized black holes with the

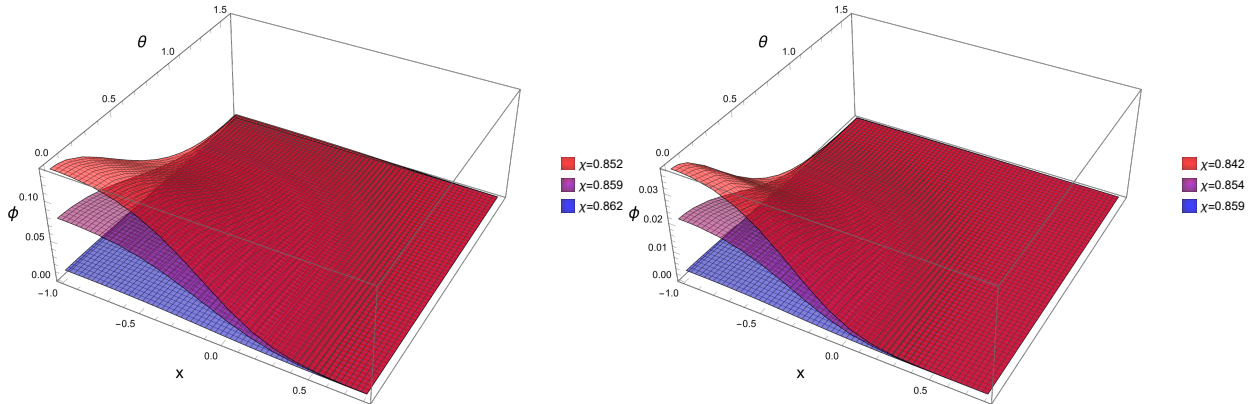


FIG. 2. Scalar field wave function $\phi(x, \theta)$ for representative scalarized black holes along the black solid lines in Fig. 1 for $\alpha = -100$ (Left Panel) and $\alpha = -1000$ (Right Panel). The scalar field corresponding to the critical scalarized black hole at point B_1 is highlighted in red and exhibits the largest amplitude. As the black hole solution approaches the bifurcation line, the scalar field amplitude decreases. In all cases, the scalar field wave functions are concentrated near the black hole poles and decay with increasing distance from the event horizon.

same q and χ , suggesting that KN black holes are slightly entropically favored over scalarized black holes. In contrast, for $\alpha > 0$, scalarized KN black holes coexist with unstable KN black holes and are always entropically favored within the coexistence region [39].

Fig. 2 presents representative scalar wave functions $\phi(x, \theta)$ for $\alpha = -100$ and -1000 . Three scalarized black hole solutions along the constant- q line connecting B_1 and B_2 , are selected. All scalar wave functions exhibit maxima near the black hole poles and decay outward from the event horizon, consistent with the fundamental scalar cloud wave functions reported in [54]. Notably, rapidly rotating KN black holes with $\alpha > 0$ develop equatorial-plane scalar cloud concentrations [56], contrasting the polar concentrations observed here. As the black hole spin decreases (i.e., approaching the critical line), scalar field amplitudes intensify near the horizon and poles. The scalarized black hole on the critical line exhibits the largest scalar field amplitude. Additionally, the amplitude of the scalar field is significantly higher for $\alpha = -100$ compared to $\alpha = -1000$.

To quantify the energy stored in the scalar field outside the event horizon, we define

$$E_\phi = \int_{r_H}^{\infty} n^\mu n^\nu T_{\mu\nu}^\phi dV, \quad (18)$$

where $T_{\mu\nu}^\phi = \partial_\mu \phi \partial_\nu \phi - g_{\mu\nu} (\partial\phi)^2 / 2$ is the stress-energy tensor of the scalar field, and n^α is the unit normal vector to spatial hypersurfaces in the 3 + 1 decomposition of spacetime. In Fig. 3, we

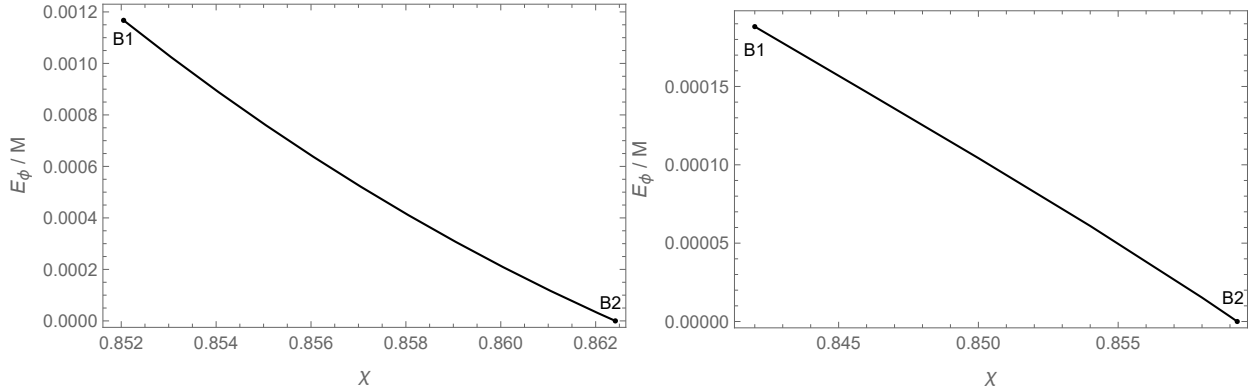


FIG. 3. Ratio of scalar field energy to black hole mass, E_ϕ/M , as a function of χ along the black solid lines in Fig. 1. **Left Panel:** $\alpha = -100$. **Right Panel:** $\alpha = -1000$. The critical scalarized black hole at point B_1 stores the largest amount of energy in the scalar field, while the black hole on the bifurcation line at point B_2 has zero scalar field energy.

present E_ϕ as a function of χ for scalarized black holes on the constant- q line connecting B_1 to B_2 , for $\alpha = -100$ and -1000 . The results show that the scalar field energy increases as χ decreases (i.e., approaching the critical line). Furthermore, E_ϕ constitutes only a small fraction of the black hole mass M , on the order of 10^{-3} for $\alpha = -100$ and 10^{-4} for $\alpha = -1000$. This suggests that the backreaction of the scalar field on the spacetime geometry is limited. Consequently, scalarized KN black hole solutions do not significantly deviate from KN black holes with scalar cloud along the bifurcation line. This limited deviation may help explain the considerably smaller domain of existence compared to cases with positive coupling. Moreover, the suppressed nonlinear effects of the scalar field also imply that terms beyond quadratic order in the series expansion of $f(\phi)$, given in Eq. (4), do not contribute significantly. This, in turn, suggests similarities in the features of scalarized black holes across different coupling functions. Indeed, Appendix B demonstrates that the existence domains for scalarized black holes are quite similar for both exponential and quadratic coupling functions.

Compared to scalarized KN black holes with $\alpha > 0$ discussed in [39], the $\alpha < 0$ case exhibits two notable distinctions: (1) the scalar field energy is substantially smaller, and (2) scalarized KN black holes coexist with stable KN black holes, rather than unstable ones. To understand these differences, consider the dynamical evolution of an unstable KN black hole undergoing a tachyonic instability, and assume that the end state of this evolution is a scalarized KN black hole¹. During the evolution, the scalar field accumulates outside the event horizon, while scalar,

¹ Other final states of the dynamical evolution are also possible. For instance, an unstable KN black hole may

electromagnetic and gravitational radiation carry away energy and angular momentum to infinity. Since the scalar field is electrically neutral, the total charge of the system remains conserved—an observation supported by fully nonlinear simulations of Reissner-Nordström (RN) black holes evolving into scalarized RN black holes [60]. Furthermore, it has been shown that slower spin enhances (suppresses) the tachyonic instability for the $\alpha > 0$ ($\alpha < 0$) case [54, 56]. At least during the early stages of the evolution, the spacetime remains well approximated by a KN black hole. Consequently, in the $\alpha > 0$ case, angular momentum loss accelerates scalar field condensation, whereas in the $\alpha < 0$ case, it hinders the process. As a result, the final scalarized KN black hole in the $\alpha < 0$ scenario is expected to deviate less from the initial KN black hole, which may account for the significantly lower scalar field energy. Moreover, for $\alpha < 0$, if the final scalarized KN black hole coexists with a KN black hole having the same global charges, the coexisting KN black hole possesses less angular momentum—and therefore a weaker tachyonic instability—than the initial (unstable) KN black hole. This reduction in angular momentum may stabilize the coexisting KN black hole, explaining why scalarized KN black holes with $\alpha < 0$ can coexist with stable KN black holes.

IV. CONCLUSIONS

In this work, we have investigated the scalarization of KN black holes within the EMS models, which exhibit a spin-induced tachyonic instability for negative coupling constants, as identified in [52, 61]. By numerically constructing spin-induced scalarized KN black hole solutions for both exponential and quadratic coupling functions, we analyzed their domain of existence and physical properties in the (χ, q) parameter space. Our results show that slowly rotating stationary black holes in these models are well described by the KN metric, whereas rapidly rotating ones develop scalar hair. Additionally, we found that the scalar field energy constitutes only a small fraction of the total black hole mass, indicating suppressed nonlinear effects of the scalar field during scalarization. This provides a plausible explanation for the relatively narrow domain of existence of scalarized black hole solutions and the similarity between solutions obtained with different coupling functions.

Notably, our analysis reveals that spin-induced scalarized KN black holes coexist with linearly stable KN black holes. This coexistence may be attributed to the loss of angular momentum during the scalarization of unstable KN black holes. If scalarized KN black holes represent the evolve into a spun-down, stable KN black hole surrounded by a scalar cloud, which is eventually depleted through electromagnetic and gravitational wave emission or other dissipative processes.

final state of scalarization, then the coexisting KN black holes must have lower angular momentum than the initial unstable ones. As the spin-induced tachyonic instability is suppressed at lower spin, the coexisting KN black holes could be stabilized, provided the angular momentum loss is sufficiently large. Electromagnetic radiation may play an important role in achieving this loss, as electromagnetic wave emission is significantly more efficient than gravitational wave emission in radiating energy and angular momentum when the black hole charge is comparable to its mass.

Furthermore, in contrast to the EsGB theories where spin-induced scalarized black holes are entropically favored, we found that, in the EMS models, KN black holes possess higher entropy in the coexisting region. Although entropic preference does not necessarily align with dynamical stability due to dissipative processes, this observation suggests that spin-induced scalarized KN black holes might be metastable and could eventually decay into stable KN black holes.

To better understand these phenomena, future investigations should address two open questions: (1) the linear stability of spin-induced scalarized KN black holes against radial and nonaxisymmetric perturbations, and (2) the nonlinear dynamical evolution of spin-induced scalarization. Resolving these issues will clarify whether spin-induced scalarized KN black holes represent a transient phase in black hole evolution or a persistent configuration, with implications for gravitational wave astronomy and high-energy astrophysics.

ACKNOWLEDGMENTS

We are grateful to Yiqian Chen for useful discussions and valuable comments. This work is supported in part by NSFC (Grant Nos. 12105191, 12275183, 12275184, 11875196, 12347133 and 12250410250).

Appendix A: Convergence Tests

To assess the numerical accuracy of our scalarized black hole solutions, we perform convergence tests by evaluating the absence of conical singularities and verifying the Smarr relation. Specifically, we define the conical singularity error as $E_C = \max_{-1 \leq x \leq 1} |F_1(x, 0) - F_2(x, 0)|$ and the Smarr relation error as $E_S = |1 - (2T_H S + 2\Omega_H J + \Phi Q) / M|$. Figs. 4 and 5 show logarithmic plots of these errors as functions of N_x (with $N_\theta = 11$) and N_θ (with $N_x = 40$), respectively. The left, middle and right columns correspond to scalarized black holes near the bifurcation line, between the bifurcation and critical lines and on the critical line, respectively. These results demonstrate exponential

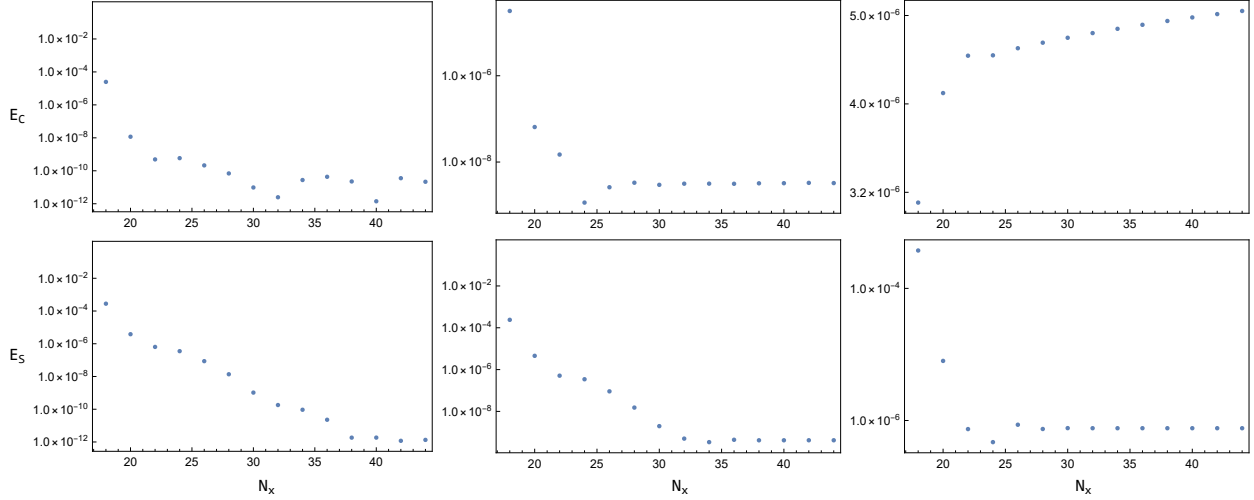


FIG. 4. Logarithmic plots of the conical singularity error E_C (**Upper Row**) and the Smarr relation error E_S (**Lower Row**) as functions of the radial resolution N_x , with fixed angular resolution $N_\theta = 11$, for scalarized black holes near the bifurcation line (**Left Column**), between the bifurcation and critical lines (**Middle Column**) and on the critical line (**Right Column**).

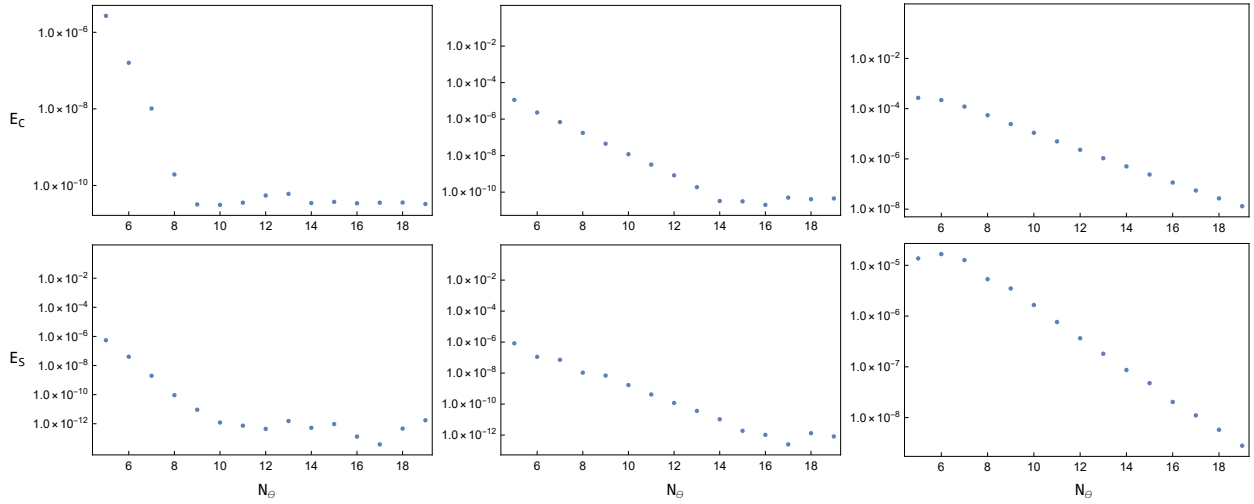


FIG. 5. Logarithmic plots of the conical singularity error E_C (**Upper Row**) and the Smarr relation error E_S (**Lower Row**) as functions of the angular resolution N_θ , with fixed radial resolution $N_x = 40$, for scalarized black holes near the bifurcation line (**Left Column**), between the bifurcation and critical lines (**Middle Column**) and on the critical line (**Right Column**).

convergence of the numerical errors, followed by round-off plateaus¹. Notably, the round-off plateau for E_S typically occurs later than for E_C . In particular, for the scalarized black hole near the bifurcation line, E_S reaches the plateau at $N_x = 40$ and $N_\theta = 11$. Based on these findings, we

¹ In the upper-right panel of Fig. 4, the conical singularity error E_C for the critical scalarized black hole has already reached a plateau within the plotted range of the resolution N_x .

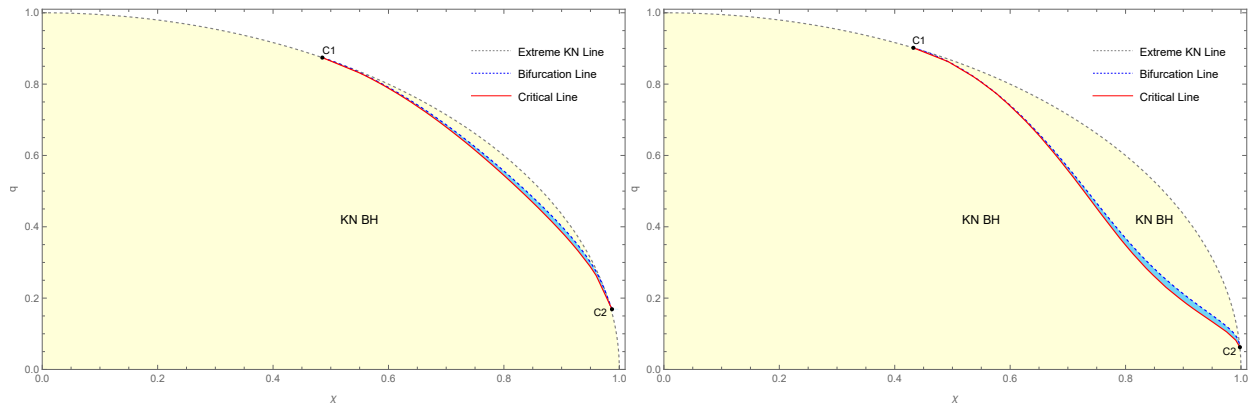


FIG. 6. Domain of existence for spin-induced scalarized KN black holes in the (χ, q) plane with the quadratic coupling function $f(\phi) = 1 + \alpha\phi^2$. **Left Panel:** $\alpha = -100$. **Right Panel:** $\alpha = -1000$.

employ spectral methods with resolutions $N_x = 40$ and $N_\theta = 11$ to solve the partial differential equations, ensuring both numerical precision and computational efficiency.

Appendix B: Quadratic Coupling Function

In this appendix, we consider the quadratic coupling function $f(\phi) = 1 + \alpha\phi^2$. The domain of existence for spin-induced scalarized black hole solutions in this case closely resembles that obtained with the exponential coupling function, indicating that the specific form of the coupling function does not significantly affect the structure of scalarized black hole solutions. As shown in Sec. III, the scalar field contributes only a small fraction to the total energy and therefore plays a limited role in determining the background geometry. The similarity in the existence domains for different coupling functions may be attributed to the suppressed nonlinear effects of the scalar field.

-
- [1] B. P. Abbott et al. Observation of Gravitational Waves from a Binary Black Hole Merger. *Phys. Rev. Lett.*, 116(6):061102, 2016. [arXiv:1602.03837](https://arxiv.org/abs/1602.03837), [doi:10.1103/PhysRevLett.116.061102](https://doi.org/10.1103/PhysRevLett.116.061102). I
 - [2] Kazunori Akiyama et al. First M87 Event Horizon Telescope Results. I. The Shadow of the Supermassive Black Hole. *Astrophys. J. Lett.*, 875:L1, 2019. [arXiv:1906.11238](https://arxiv.org/abs/1906.11238), [doi:10.3847/2041-8213/ab0ec7](https://doi.org/10.3847/2041-8213/ab0ec7). I
 - [3] Kazunori Akiyama et al. First M87 Event Horizon Telescope Results. II. Array and Instrumentation. *Astrophys. J. Lett.*, 875(1):L2, 2019. [arXiv:1906.11239](https://arxiv.org/abs/1906.11239), [doi:10.3847/2041-8213/ab0c96](https://doi.org/10.3847/2041-8213/ab0c96).

- [4] Kazunori Akiyama et al. First M87 Event Horizon Telescope Results. III. Data Processing and Calibration. *Astrophys. J. Lett.*, 875(1):L3, 2019. [arXiv:1906.11240](#), [doi:10.3847/2041-8213/ab0c57](#).
- [5] Kazunori Akiyama et al. First M87 Event Horizon Telescope Results. IV. Imaging the Central Supermassive Black Hole. *Astrophys. J. Lett.*, 875(1):L4, 2019. [arXiv:1906.11241](#), [doi:10.3847/2041-8213/ab0e85](#).
- [6] Kazunori Akiyama et al. First M87 Event Horizon Telescope Results. V. Physical Origin of the Asymmetric Ring. *Astrophys. J. Lett.*, 875(1):L5, 2019. [arXiv:1906.11242](#), [doi:10.3847/2041-8213/ab0f43](#).
- [7] Kazunori Akiyama et al. First M87 Event Horizon Telescope Results. VI. The Shadow and Mass of the Central Black Hole. *Astrophys. J. Lett.*, 875(1):L6, 2019. [arXiv:1906.11243](#), [doi:10.3847/2041-8213/ab1141](#).
- [8] Kazunori Akiyama et al. First M87 Event Horizon Telescope Results. VII. Polarization of the Ring. *Astrophys. J. Lett.*, 910(1):L12, 2021. [arXiv:2105.01169](#), [doi:10.3847/2041-8213/abe71d](#).
- [9] Kazunori Akiyama et al. First M87 Event Horizon Telescope Results. VIII. Magnetic Field Structure near The Event Horizon. *Astrophys. J. Lett.*, 910(1):L13, 2021. [arXiv:2105.01173](#), [doi:10.3847/2041-8213/abe4de](#).
- [10] Kazunori Akiyama et al. First Sagittarius A* Event Horizon Telescope Results. I. The Shadow of the Supermassive Black Hole in the Center of the Milky Way. *Astrophys. J. Lett.*, 930(2):L12, 2022. [doi:10.3847/2041-8213/ac6674](#).
- [11] Kazunori Akiyama et al. First Sagittarius A* Event Horizon Telescope Results. II. EHT and Multiwavelength Observations, Data Processing, and Calibration. *Astrophys. J. Lett.*, 930(2):L13, 2022. [doi:10.3847/2041-8213/ac6675](#).
- [12] Kazunori Akiyama et al. First Sagittarius A* Event Horizon Telescope Results. III. Imaging of the Galactic Center Supermassive Black Hole. *Astrophys. J. Lett.*, 930(2):L14, 2022. [doi:10.3847/2041-8213/ac6429](#).
- [13] Kazunori Akiyama et al. First Sagittarius A* Event Horizon Telescope Results. IV. Variability, Morphology, and Black Hole Mass. *Astrophys. J. Lett.*, 930(2):L15, 2022. [doi:10.3847/2041-8213/ac6736](#).
- [14] Kazunori Akiyama et al. First Sagittarius A* Event Horizon Telescope Results. V. Testing Astrophysical Models of the Galactic Center Black Hole. *Astrophys. J. Lett.*, 930(2):L16, 2022. [doi:10.3847/2041-8213/ac6672](#).
- [15] Kazunori Akiyama et al. First Sagittarius A* Event Horizon Telescope Results. VI. Testing the Black Hole Metric. *Astrophys. J. Lett.*, 930(2):L17, 2022. [doi:10.3847/2041-8213/ac6756](#). I
- [16] Werner Israel. Event horizons in static vacuum space-times. *Phys. Rev.*, 164:1776–1779, 1967. [doi:10.1103/PhysRev.164.1776](#). I
- [17] B. Carter. Axisymmetric Black Hole Has Only Two Degrees of Freedom. *Phys. Rev. Lett.*, 26:331–333, 1971. [doi:10.1103/PhysRevLett.26.331](#).

- [18] Remo Ruffini and John A. Wheeler. Introducing the black hole. *Phys. Today*, 24(1):30, 1971. [doi:10.1063/1.3022513](https://doi.org/10.1063/1.3022513). I
- [19] M.S. Volkov and D.V. Galtsov. NonAbelian Einstein Yang-Mills black holes. *JETP Lett.*, 50:346–350, 1989. I
- [20] P. Bizon. Colored black holes. *Phys. Rev. Lett.*, 64:2844–2847, 1990. [doi:10.1103/PhysRevLett.64.2844](https://doi.org/10.1103/PhysRevLett.64.2844).
- [21] Brian R. Greene, Samir D. Mathur, and Christopher M. O’Neill. Eluding the no hair conjecture: Black holes in spontaneously broken gauge theories. *Phys. Rev. D*, 47:2242–2259, 1993. [arXiv:hep-th/9211007](https://arxiv.org/abs/hep-th/9211007), [doi:10.1103/PhysRevD.47.2242](https://doi.org/10.1103/PhysRevD.47.2242). I
- [22] Hugh Luckock and Ian Moss. BLACK HOLES HAVE SKYRMION HAIR. *Phys. Lett. B*, 176:341–345, 1986. [doi:10.1016/0370-2693\(86\)90175-9](https://doi.org/10.1016/0370-2693(86)90175-9). I
- [23] Serge Droz, Markus Heusler, and Norbert Straumann. New black hole solutions with hair. *Phys. Lett. B*, 268:371–376, 1991. [doi:10.1016/0370-2693\(91\)91592-J](https://doi.org/10.1016/0370-2693(91)91592-J). I
- [24] P. Kanti, N.E. Mavromatos, J. Rizos, K. Tamvakis, and E. Winstanley. Dilatonic black holes in higher curvature string gravity. *Phys. Rev. D*, 54:5049–5058, 1996. [arXiv:hep-th/9511071](https://arxiv.org/abs/hep-th/9511071), [doi:10.1103/PhysRevD.54.5049](https://doi.org/10.1103/PhysRevD.54.5049). I
- [25] Carlos A.R. Herdeiro and Eugen Radu. Asymptotically flat black holes with scalar hair: a review. *Int. J. Mod. Phys. D*, 24(09):1542014, 2015. [arXiv:1504.08209](https://arxiv.org/abs/1504.08209), [doi:10.1142/S0218271815420146](https://doi.org/10.1142/S0218271815420146). I
- [26] Thibault Damour and Gilles Esposito-Farese. Nonperturbative strong field effects in tensor - scalar theories of gravitation. *Phys. Rev. Lett.*, 70:2220–2223, 1993. [doi:10.1103/PhysRevLett.70.2220](https://doi.org/10.1103/PhysRevLett.70.2220). I
- [27] Thibault Damour and Gilles Esposito-Farese. Tensor - scalar gravity and binary pulsar experiments. *Phys. Rev. D*, 54:1474–1491, 1996. [arXiv:gr-qc/9602056](https://arxiv.org/abs/gr-qc/9602056), [doi:10.1103/PhysRevD.54.1474](https://doi.org/10.1103/PhysRevD.54.1474).
- [28] Vitor Cardoso, Isabella P. Carucci, Paolo Pani, and Thomas P. Sotiriou. Matter around Kerr black holes in scalar-tensor theories: scalarization and superradiant instability. *Phys. Rev. D*, 88:044056, 2013. [arXiv:1305.6936](https://arxiv.org/abs/1305.6936), [doi:10.1103/PhysRevD.88.044056](https://doi.org/10.1103/PhysRevD.88.044056).
- [29] Vitor Cardoso, Isabella P. Carucci, Paolo Pani, and Thomas P. Sotiriou. Black holes with surrounding matter in scalar-tensor theories. *Phys. Rev. Lett.*, 111:111101, 2013. [arXiv:1308.6587](https://arxiv.org/abs/1308.6587), [doi:10.1103/PhysRevLett.111.111101](https://doi.org/10.1103/PhysRevLett.111.111101). I
- [30] Alexandru Dima, Enrico Barausse, Nicola Franchini, and Thomas P. Sotiriou. Spin-induced black hole spontaneous scalarization. *Phys. Rev. Lett.*, 125(23):231101, 2020. [arXiv:2006.03095](https://arxiv.org/abs/2006.03095), [doi:10.1103/PhysRevLett.125.231101](https://doi.org/10.1103/PhysRevLett.125.231101). I
- [31] Carlos A. R. Herdeiro, Eugen Radu, Hector O. Silva, Thomas P. Sotiriou, and Nicolás Yunes. Spin-induced scalarized black holes. *Phys. Rev. Lett.*, 126(1):011103, 2021. [arXiv:2009.03904](https://arxiv.org/abs/2009.03904), [doi:10.1103/PhysRevLett.126.011103](https://doi.org/10.1103/PhysRevLett.126.011103). I, IIB, IIB
- [32] Emanuele Berti, Lucas G. Collodel, Burkhard Kleihaus, and Jutta Kunz. Spin-induced black-hole scalarization in Einstein-scalar-Gauss-Bonnet theory. *Phys. Rev. Lett.*, 126(1):011104, 2021. [arXiv:2009.03905](https://arxiv.org/abs/2009.03905), [doi:10.1103/PhysRevLett.126.011104](https://doi.org/10.1103/PhysRevLett.126.011104). I

- [33] Carlos A.R. Herdeiro, Eugen Radu, Nicolas Sanchis-Gual, and José A. Font. Spontaneous Scalarization of Charged Black Holes. *Phys. Rev. Lett.*, 121(10):101102, 2018. [arXiv:1806.05190](#), [doi:10.1103/PhysRevLett.121.101102](#). I
- [34] Pedro G. S. Fernandes, Carlos A. R. Herdeiro, Alexandre M. Pombo, Eugen Radu, and Nicolas Sanchis-Gual. Spontaneous Scalarisation of Charged Black Holes: Coupling Dependence and Dynamical Features. *Class. Quant. Grav.*, 36(13):134002, 2019. [Erratum: *Class.Quant.Grav.* 37, 049501 (2020)]. [arXiv:1902.05079](#), [doi:10.1088/1361-6382/ab23a1](#). I
- [35] Pedro G.S. Fernandes, Carlos A.R. Herdeiro, Alexandre M. Pombo, Eugen Radu, and Nicolas Sanchis-Gual. Charged black holes with axionic-type couplings: Classes of solutions and dynamical scalarization. *Phys. Rev. D*, 100(8):084045, 2019. [arXiv:1908.00037](#), [doi:10.1103/PhysRevD.100.084045](#).
- [36] Jose Luis Blázquez-Salcedo, Carlos A.R. Herdeiro, Jutta Kunz, Alexandre M. Pombo, and Eugen Radu. Einstein-Maxwell-scalar black holes: the hot, the cold and the bald. *Phys. Lett. B*, 806:135493, 2020. [arXiv:2002.00963](#), [doi:10.1016/j.physletb.2020.135493](#).
- [37] Peng Wang, Houwen Wu, and Haitang Yang. Scalarized Einstein-Born-Infeld black holes. *Phys. Rev. D*, 103(10):104012, 2021. [arXiv:2012.01066](#), [doi:10.1103/PhysRevD.103.104012](#).
- [38] Guangzhou Guo, Peng Wang, Houwen Wu, and Haitang Yang. Scalarized Einstein–Maxwell-scalar black holes in anti-de Sitter spacetime. *Eur. Phys. J. C*, 81(10):864, 2021. [arXiv:2102.04015](#), [doi:10.1140/epjc/s10052-021-09614-7](#). IIB
- [39] Guangzhou Guo, Peng Wang, Houwen Wu, and Haitang Yang. Scalarized Kerr-Newman black holes. *JHEP*, 10:076, 2023. [arXiv:2307.12210](#), [doi:10.1007/JHEP10\(2023\)076](#). I, IIB, III, III
- [40] Qingyu Gan, Peng Wang, Houwen Wu, and Haitang Yang. Photon ring and observational appearance of a hairy black hole. *Phys. Rev. D*, 104(4):044049, 2021. [arXiv:2105.11770](#), [doi:10.1103/PhysRevD.104.044049](#). I
- [41] Qingyu Gan, Peng Wang, Houwen Wu, and Haitang Yang. Photon spheres and spherical accretion image of a hairy black hole. *Phys. Rev. D*, 104(2):024003, 2021. [arXiv:2104.08703](#), [doi:10.1103/PhysRevD.104.024003](#). I
- [42] Guangzhou Guo, Xin Jiang, Peng Wang, and Houwen Wu. Gravitational lensing by black holes with multiple photon spheres. *Phys. Rev. D*, 105(12):124064, 2022. [arXiv:2204.13948](#), [doi:10.1103/PhysRevD.105.124064](#).
- [43] Yiqian Chen, Guangzhou Guo, Peng Wang, Houwen Wu, and Haitang Yang. Appearance of an infalling star in black holes with multiple photon spheres. *Sci. China Phys. Mech. Astron.*, 65(12):120412, 2022. [arXiv:2206.13705](#), [doi:10.1007/s11433-022-1986-x](#).
- [44] Yiqian Chen, Peng Wang, and Haitang Yang. Interferometric Signatures of Black Holes with Multiple Photon Spheres. 12 2023. [arXiv:2312.10304](#).
- [45] Yiqian Chen, Peng Wang, and Haitang Yang. Observations of orbiting hot spots around scalarized Reissner–Nordström black holes. *Eur. Phys. J. C*, 84(3):270, 2024. [arXiv:2401.10905](#), [doi:10.1140/epjc/s10052-024-12635-7](#). I

- [46] Vitor Cardoso, Luís C. B. Crispino, Caio F. B. Macedo, Hirotada Okawa, and Paolo Pani. Light rings as observational evidence for event horizons: long-lived modes, ergoregions and nonlinear instabilities of ultracompact objects. *Phys. Rev. D*, 90(4):044069, 2014. [arXiv:1406.5510](#), [doi:10.1103/PhysRevD.90.044069](#). I
- [47] Joe Keir. Slowly decaying waves on spherically symmetric spacetimes and ultracompact neutron stars. *Class. Quant. Grav.*, 33(13):135009, 2016. [arXiv:1404.7036](#), [doi:10.1088/0264-9381/33/13/135009](#).
- [48] Minyong Guo, Zhen Zhong, Jinguang Wang, and Sijie Gao. Light rings and long-lived modes in quasiblack hole spacetimes. *Phys. Rev. D*, 105(2):024049, 2022. [arXiv:2108.08967](#), [doi:10.1103/PhysRevD.105.024049](#).
- [49] Guangzhou Guo, Peng Wang, Houwen Wu, and Haitang Yang. Quasinormal modes of black holes with multiple photon spheres. *JHEP*, 06:060, 2022. [arXiv:2112.14133](#), [doi:10.1007/JHEP06\(2022\)060](#).
- [50] Guangzhou Guo, Peng Wang, Houwen Wu, and Haitang Yang. Echoes from hairy black holes. *JHEP*, 06:073, 2022. [arXiv:2204.00982](#), [doi:10.1007/JHEP06\(2022\)073](#). I
- [51] Guangzhou Guo, Peng Wang, Houwen Wu, and Haitang Yang. Superradiance instabilities of charged black holes in Einstein-Maxwell-scalar theory. *JHEP*, 07:070, 2023. [arXiv:2301.06483](#), [doi:10.1007/JHEP07\(2023\)070](#). I
- [52] Shahar Hod. Spin-charge induced scalarization of Kerr-Newman black-hole spacetimes. *JHEP*, 08:272, 2022. [arXiv:2206.12074](#), [doi:10.1007/JHEP08\(2022\)272](#). I, IV
- [53] Meng-Yun Lai, Yun Soo Myung, Rui-Hong Yue, and De-Cheng Zou. Spin-charge induced spontaneous scalarization of Kerr-Newman black holes. *Phys. Rev. D*, 106(8):084043, 2022. [arXiv:2208.11849](#), [doi:10.1103/PhysRevD.106.084043](#). I
- [54] Guangzhou Guo, Peng Wang, Tianshu Wu, and Haitang Yang. Spin-induced Scalar Clouds around Kerr-Newman Black Holes. 8 2024. [arXiv:2409.04458](#). I, II A, II A, III, III
- [55] Oscar J. C. Dias, Mahdi Godazgar, and Jorge E. Santos. Linear Mode Stability of the Kerr-Newman Black Hole and Its Quasinormal Modes. *Phys. Rev. Lett.*, 114(15):151101, 2015. [arXiv:1501.04625](#), [doi:10.1103/PhysRevLett.114.151101](#). II A
- [56] Guangzhou Guo, Peng Wang, Tianshu Wu, and Haitang Yang. Stationary scalar clouds around Kerr-Newman black holes. *JHEP*, 11:065, 2024. [arXiv:2408.09243](#), [doi:10.1007/JHEP11\(2024\)065](#). II A, II A, III, III
- [57] Carlos Herdeiro and Eugen Radu. Construction and physical properties of Kerr black holes with scalar hair. *Class. Quant. Grav.*, 32(14):144001, 2015. [arXiv:1501.04319](#), [doi:10.1088/0264-9381/32/14/144001](#). II B, II B, II B, II B, II B
- [58] Jorge F. M. Delgado, Carlos A. R. Herdeiro, Eugen Radu, and Helgi Runarsson. Kerr-Newman black holes with scalar hair. *Phys. Lett. B*, 761:234–241, 2016. [arXiv:1608.00631](#), [doi:10.1016/j.physletb.2016.08.032](#). II B, II B

- [59] Pedro G. S. Fernandes and David J. Mulryne. A new approach and code for spinning black holes in modified gravity. *Class. Quant. Grav.*, 40(16):165001, 2023. [arXiv:2212.07293](#), [doi:10.1088/1361-6382/ace232](#). II B
- [60] Sebastian Garcia-Saenz, Guangzhou Guo, Peng Wang, and Xinmiao Wang. Hairless Black Hole by Superradiance. 2 2025. [arXiv:2502.18003](#). III
- [61] Meng-Yun Lai, Yun Soo Myung, Rui-Hong Yue, and De-Cheng Zou. Spin-induced scalarization of Kerr-Newman black holes in Einstein-Maxwell-scalar theory. *Phys. Rev. D*, 106(4):044045, 2022. [arXiv:2206.11587](#), [doi:10.1103/PhysRevD.106.044045](#). IV